Journal of Hydrology: Regional Studies 52 (2024) 101712

Contents lists available at ScienceDirect

Journal of Hydrology: Regional Studies

journal homepage: www.elsevier.com/locate/ejrh

Diverse spatiotemporal patterns of vapor pressure deficit and soil moisture across China

Shanshan Chen [a,b], Songlin Zhang [a], Shengjun Wu [a,*]

[a] Key Laboratory of Reservoir Aquatic Environment, Chongqing Institute of Green and Intelligent Technology, Chinese Academy of Sciences, Chongqing 400714, China

[b] CAS Key Laboratory of Tropical Forest Ecology, Xishuangbanna Tropical Botanical Graden, Chinese Academy of Sciences, Mengla, Yunnan, China

ARTICLE INFO

Keywords:
EOF
VPD
Surface soil moisture
Root-zone soil moisture
Different climate zones

ABSTRACT

Study region: China and the different climatic zones.
Study focus: Vapor pressure deficit (VPD) and soil moisture (SM) are vital for the land-atmosphere hydrological cycle and vegetation growth. Understanding the spatiotemporal variations of VPD and SM is essential for exploring vegetation dynamics and ecosystem changes. However, our current understanding of the simultaneous variations of VPD and SM within specific regions remains limited. This study utilized Empirical Orthogonal Function (EOF) methods to analyze the spatiotemporal variability of VPD, surface SM (SM_{surf}), and root-zone SM (SM_{root}), respectively. We then investigated the synchronous and asynchronous variations of VPD and SM and examined their relationships with climatic factors.
New hydrologic insights for the region: From 1980–2020, VPD exhibited a significant upward trend across China and in various climate zones, indicating an increase in atmospheric dryness. However, the trends of SM_{surf} and SM_{root} showed a slight upward trend across China but divergent patterns in different climate zones. In summary, approximately 43% of China experiences a significant simultaneous increase in both VPD and SM, mainly in semi-arid and arid regions. Conversely, about 4% of China shows contrasting changes in VPD and SM, primarily in humid tropical and subtropical regions. These findings enhance our understanding of VPD and SM patterns in various climates, emphasizing the significance of soil drought in humid and semi-humid regions.

1. Introduction

Water deficit can be categorized as atmosphere water deficit or soil water deficit. Vapor pressure deficit (VPD) and soil moisture (SM) are key indicators used to evaluate the status of atmosphere and soil water, respectively. VPD is a critical determinant of the atmospheric demand for water vapor and exerts a pivotal influence on the water balance dynamics within the atmosphere. It represents the difference between saturated vapor pressure (SVP) and actual vapor pressure (AVP) (Fang et al., 2022). While SVP is determined solely by air temperature (De Boeck et al., 2010), AVP is influenced by multiple factors, including air temperature, air humidity, evaporation, and SM, among others (Fang et al., 2022; Ficklin and Novick, 2017). As a result, SVP and AVP exhibit different rates of change with increasing air temperature. Typically, the growth rates of AVP tend to lag behind those of SVP, resulting in an elevation of

* Corresponding author.
E-mail address: wsj@cigit.ac.cn (S. Wu).

https://doi.org/10.1016/j.ejrh.2024.101712
Received 4 July 2023; Received in revised form 28 January 2024; Accepted 20 February 2024
Available online 22 February 2024
2214-5818/

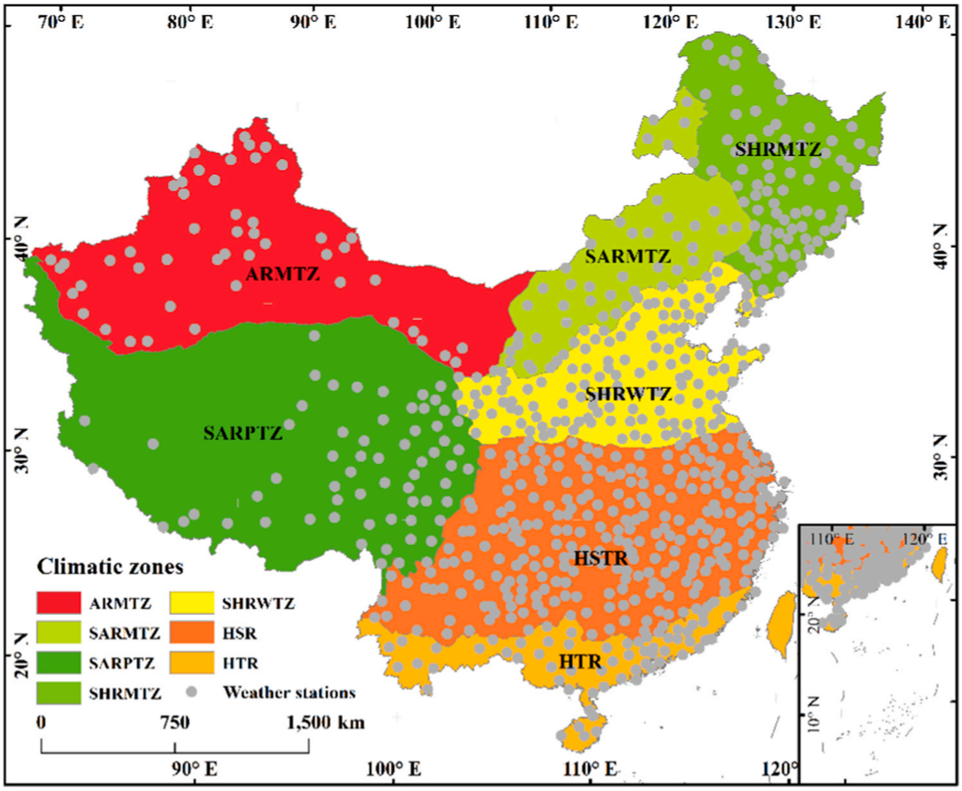

Fig. 1. Climate zones and distribution of meteorological stations. Arid regions in the middle-temperature zone: ARMTZ; Semi-arid regions in the middle-temperature zone: SARMTZ; Semi-humid regions in the middle-temperature zone: SHRMTZ; Semi-arid regions in the Plateau temperature zone: SARPTZ; Semi-humid regions in the warm temperature zone: SHRWTZ; Humid subtropical regions: HSTR; Humid tropical regions: HTR.

VPD. This variability in VPD exerts diverse impacts on vegetation productivity (Yuan et al., 2019). For example, high VPD causes vegetation to close stomata, affecting photosynthesis and potentially leading to water scarcity in plants (Sangines de Carcer et al., 2018). Furthermore, SM is a reliable indicator of soil water availability, playing an essential role in plant growth (Gatti et al., 2014; Yu et al., 2022). Variability in SM directly influences plant water availability, thereby holding substantial implications for plant growth (Stocker et al., 2018; Zhang et al., 2022b), diversity (Deng et al., 2016; Winkler et al., 2016), and productivity (Wei et al., 2018). In sub-humid, semi-arid, or arid regions, the considerable effects of SM alone can lead to a reduction in gross primary productivity by up to 40% (Stocker et al., 2018). Moreover, surface soil moisture (SM_{surf}) has a greater influence on productivity. For instance, a significant and positive correlation was observed between the below-ground biomass of native grasslands and moisture content in the top 10 cm layer of soil across the Loess Plateau (Deng et al., 2016). SM can reduce gross primary production through ecosystem water stress and contribute to vegetation mortality, thereby reducing the present land carbon sink (Green et al., 2019). As previously stated, both VPD and SM play crucial roles in driving vegetation dynamics. Therefore, understanding the spatiotemporal variability of VPD and SM is imperative for a comprehensively grasping changes in vegetation ecosystems.

Numerous studies focus on the temporal-spatial dynamics of VPD or SM and their impact. Some examined changes in VPD or SM in specific regions (Berg et al., 2017; Fang et al., 2022; Ficklin and Novick, 2017; Liu and Yang, 2023) and disentangled their respective effects on vegetation, such as phenology (Chen et al., 2021) and productivity (Ameztegui et al., 2021; Lu et al., 2022; Sangines de Carcer et al., 2018; Yuan, 2019). Moreover, Other researchers analyzed the future trends of VPD or SM through the CMIP6 (Berg et al., 2017; Ficklin and Novick, 2017). Studying either VPD or SM alone leads to an incomplete understanding of drought stress in a region. Insufficient SM supply and elevated VPD are recognized as primary drivers of vegetation dryness stress. However, in the context of climate warming, it is observed that VPD is exhibiting an upward trend in a region, while the corresponding alterations in SM are undisclosed, and vice versa. This hinders our ability to gain a comprehensive understanding of regional (global) atmospheric and soil moisture conditions. Besides, capturing simultaneous changes in VPD and SM is crucial for an accurate comprehension of ecosystem drying stress and essential for effective drought risk management. Therefore, the notable knowledge gap arises due to the lack of research exploring concurrent changes in both VPD and SM within the same geographic area.

Spatial variation patterns of VPD or SM are commonly examined using linear regression analysis (Fang et al., 2022) and the Mann-Kendall (MK) test (Cheng et al., 2015; Kong et al., 2019). However, due to the non-linear nature of VPD and SM variations, the aforementioned linear methods may not fully capture the true dynamics of VPD and SM changes. To address this issue, the application of ensemble empirical mode decomposition (EEMD) can help detect non-linear trends (Cheng and Huang, 2016). Nevertheless, it may

Table 1
Datasets used in this study.

Datasets	Property	Temporal coverage	Temporal resolution	Spatial resolution	Variables (units)
-	In situ	1951–2022	Daily	-	T (°C), RH (%), SP (hPa)
ERA5-land	Reanalysis	1981–2020	Monthly	0.1° × 0.1°	T (K), Td (K), P (m), SP (Pa), E (m of water equivalent), ES (m of water equivalent), EV (m of water equivalent)
GLEAMV3.6a	Satellite and reanalysis data	1980–2020	Monthly	0.25° × 0.25°	SM_{surf} (m^3/m^{-3}), SM_{root} (m^3/m^{-3})
MERRA2	Reanalysis	1980–2020	Monthly	0.5° × 0.625°	SR (W m^{-2})

Note. T = air temperature; Td = dew point temperature; AVP = actual vapor pressure; RH = relative humidity; SR = downwelling shortwave radiation; E: total evaporation; ES: evaporation from bare soil; EV: evaporation from vegetation transpiration; P = precipitation; SP = surface pressure; SM_{surf} = surface soil moisture; SM_{root} = root-zone soil moisture.

not capture subtle interannual variability. Therefore, the need for new and more effective research methods arises to address these limitations and better capture the complexities of VPD and SM variation. Empirical orthogonal function (EOF) analysis, also referred to as eigenvector analysis, is an effective method for analyzing condensed anomalous information and revealing the spatial and temporal structure of anomalies. EOF, widely applied in meteorology (Levitus et al., 2005; Mao et al., 2021; Wang et al., 2017), employs a feature technique that separates the temporal and spatial variations of the variable field, representing them with as few modes as possible. One notable advantage of EOF is its capability to effectively compress and consolidate extensive data information. Additionally, it can decompose irregularly distributed sites within a limited area, decomposing spatial structures that possess clear physical interpretation (Wang et al., 2017). In this context, we will use the EOF method to explore the spatial and temporal variations, as well as spatial anomalies, in both VPD and SM.

In this study, we evaluated the temporal variations of VPD and SM across China and within various climatic zones using the EEMD method from 1980 to 2020. Following that, we applied the EOF method to investigate the spatial variations and anomalies of VPD and SM. Lastly, we concurrently examined the patterns of VPD and SM.

2. Materials and methods

2.1. Datasets

2.1.1. In situ data

To calculate the VPD for the period spanning from 1980 to 2020, monthly climate data comprising air temperature, pressure, and specific humidity were acquired from the China Meteorological Forcing Dataset (CMFD) (https://data.cma.cn/, Fig. 1). The meteorological station data only retained points that were consistently available from 1980 to 2020, totaling 578 points. Regarding missing data, if a station had more than 10% of data missing in a given year, the station was excluded. The final number of meteorological station data points was 498. Missing data was imputed using the average of the data from the preceding and subsequent five years.

2.1.2. ERA5-land

The reanalysis data utilized in this study was obtained from the Copernicus Climate Change Service at the European Centre for Medium-Range Weather Forecasts (https://cds.climate.copernicus.eu/cdsapp#!/search?type=dataset) (Muñoz Sabater, 2019). Specifically, we extracted land air temperature (T) and dew point temperature (Td) from the ERA5-land dataset to calculate the VPD. Various meteorological variables were collected to investigate the relationship between VPD and SM, including precipitation (P), downing incoming shortwave radiation (SR), total evaporation (E), evaporation from vegetation transpiration (EV), evaporation from bare soil (ES), soil temperature of 0–7 cm (STM), and surface pressure (SP).

2.1.3. Soil moisture (SM)

SM data were obtained from the Global Land Evaporation Amsterdam Model (GLEAM) V3.6a (https://www.gleam.eu/), including surface soil moisture (SM_{surf}) and root-zone soil moisture (SM_{root}). The GLEAM SM was generated by assimilating the data using the surface model GLEAM (Martens et al., 2017; Miralles et al., 2011), employing an optimized Newtonian light extrapolation method. The GLEAM SM products have demonstrated a high level of accuracy, with a median R value of 0.71 (Beck et al., 2021). The data cover the period from 1980 to 2020, with a spatial resolution of 0.25° × 0.25° and monthly temporal resolution.

2.1.4. MERRA2

Solar radiation was the Modern-Era Retrospective analysis for Research and Applications, version 2 (MERRA2) reanalysis data (Table 1). It was generated by NASA's Global Modeling and Assimilation Office (GMAO) using the Goddard Earth Observing System Model. We extracted monthly surface incoming shortwave flux (solar radiation) from the dataset to analyze its relationship with VPD and SM.

2.1.5. Ancillary data (DEM, climate zones)

The Digital elevation model (DEM) data were derived from the NASA Shuttle Radar Topographic Mission (SRTM), available at http://srtm.csi.cgiar.org. The DEM, produced in 2000, provides a spatial resolution of 90 m.

The climate zone is classified by the long-term average of accumulated temperature during periods with a daily mean temperature not falling below 10 °C. The long-term average of the coldest month's temperature or extreme minimum temperature serves as an indicator for heat assessment. Dryness is used as the moisture indicator and determined by climate indices. For the detailed criteria used in the division of climate zones, please refer to Table S1. Fig. 1 presents the spatial distribution of these climate zones.

2.2. Calculation of VPD

VPD was calculated using the following equations (Fang et al., 2022; Yuan, 2019).

In situ:

$$\mathrm{VPD} = 0.61078 \times e^{\frac{17.27\times T}{T\times 237.3}} \times \left(1 - RH\right) \tag{1}$$

ERA5-Land:

$$\mathrm{VPD} = \mathrm{SVP} - \mathrm{AVP} \tag{2}$$

The units of SVP, AVP, and RH are hPa, hPa, and %, respectively. SVP and AVP can be derived from the following equations:

$$\mathrm{SVP} = 6.112 \times f_w \times \exp\left(\frac{17.67\mathrm{T}}{\mathrm{T} + 243.5}\right) \tag{3}$$

$$\mathrm{AVP} = 6.112 \times f_w \times \exp\left(\frac{17.67T_\mathrm{d}}{T_d + 243.5}\right) \tag{4}$$

$$f_\mathrm{w} = 1 + 7 \times 10^{-4} + 3.46 \times 10^{-6}\mathrm{P_{mst}} \tag{5}$$

$$\mathrm{P_{mst}} = \mathrm{P_{msl}} \times \left(\frac{\mathrm{T} + 273.16}{\mathrm{T} + 273.16 + 0.0065 \times \mathrm{Z}}\right)^{5.625} \tag{6}$$

Where T, T_d, Z, P_{mst}, and P_{msl} are the air temperature (°C), dew point temperature (°C), altitude (m), air pressure (hPa), and the air pressure at the mean sea level (1013.25 hPa), respectively.

2.3. Spatiotemporal analyses

2.3.1. Time series trend analysis

(1) Sen-MK

To examine linear trends in VPD, SM_{surf}, and SM_{root} at the annual and pixel scale, we first computed the annual average of monthly VPD, SM_{surf}, and SM_{root}. The Theil-Sen median slope method was then employed to detect inter-annual variation trends in VPD, SM_{surf}, and SM_{root}. This method is robust to data distribution and insensitive to outliers, making it suitable for objectively describing the overall trend characteristics of long-term data. This method was applied to analyze the temporal variation of annual VPD, SM_{surf}, and SM_{root} using the following formula:

$$\beta = \mathrm{mean}\left(\frac{x_j - x_i}{j - i}\right), j > i \tag{7}$$

Where x_j and x_i are time series data. $\beta > 0$ shows an upward trend and $\beta < 0$ indicates a downward trend. To identify significant trends, a nonparametric statistical test (Mann-Kendall, M-K) was conducted. Furthermore, we also analyzed the changes in VPD, SM_{surf}, and SM_{root} at the biome level.

(2) Ensemble empirical mode decomposition (EEMD)

Ensemble empirical mode decomposition (EEMD) is an efficient and adaptive time-frequency analysis method for processing nonlinear and nonstationary time series. The EEMD method decomposes nonlinear and nonstationary time series data into n intrinsic mode functions (IMF: imf_i, i= 1, 2, …, n) and a residue trend (Huang et al., 1998). The detailed process of the EEMD method was described by Liu et al. (2018).

2.3.2. Spatial analysis

Empirical orthogonal function (EOF) is a widely used and effective method in atmospheric science research for analyzing the spatial and temporal variability characteristics of variables (Levitus et al., 2005). In this method, the observational data within a study area, comprising m observation points, each with n observations, can be presented in matrix form as follows:

$$X = \left(x_{ij}\right) = \left(x_1, x_2, x_3, \cdots, x_j\right) = \begin{pmatrix} x_{11} & \cdots & x_{1n} \\ \vdots & \ddots & \vdots \\ x_{m1} & \cdots & x_{m1} \end{pmatrix} \tag{8}$$

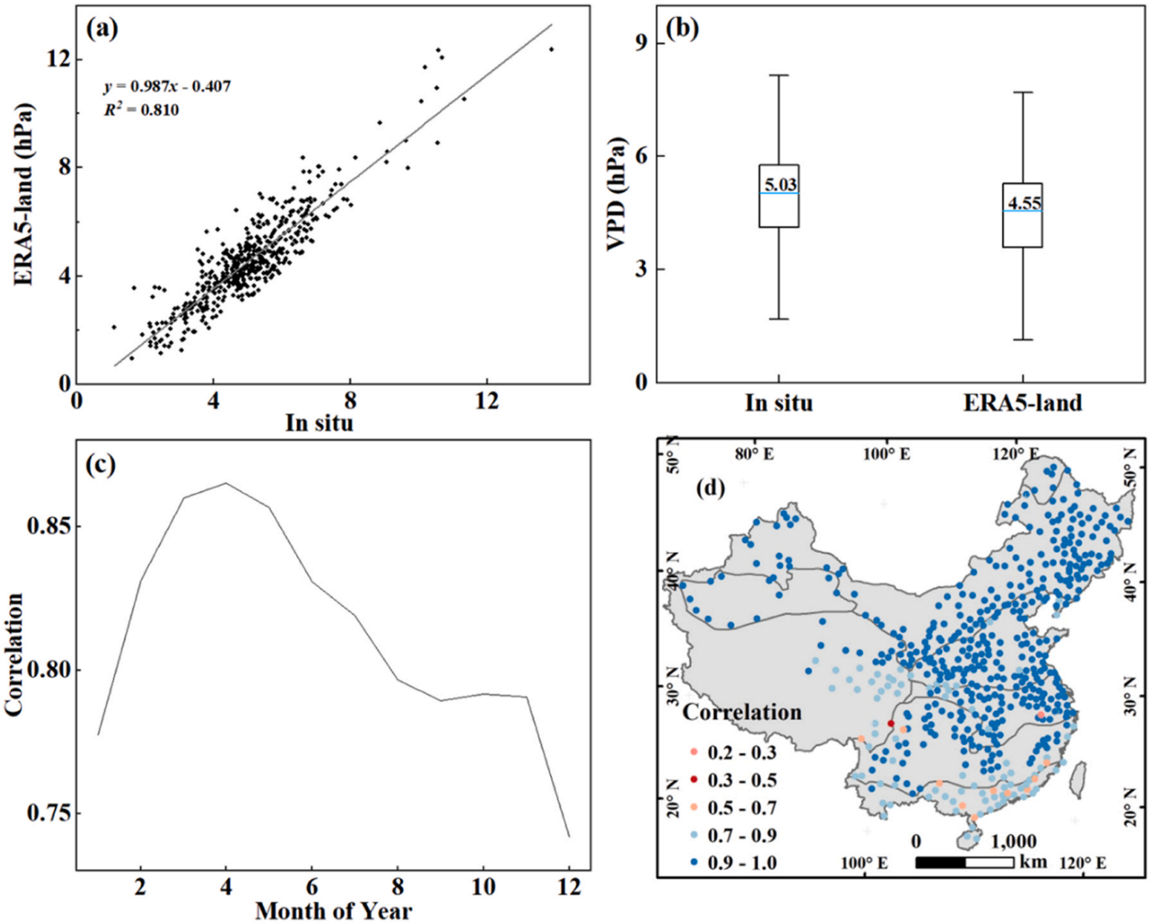

Fig. 2. Evaluation of VPD from the ERA5-land dataset, comparing it to in situ observations at a monthly scale. (a) indicates the correlation between VPD derived from the ERA5-land and in situ VPD from all stations (n = 498). (b) displays the mean VPD value from in situ data and the corresponding pixel values from ERA5-land. The green solid lines in the boxes represent the mean values. (c) indicates the variation in correlation coefficients.

Wherex_{ij}denotes the jth observation on the ith grid. m indicates the number of observation locations, while n refers to the number of observations at each location. By EOF expansion, Eq. (8) can be decomposed into the sum of the products of the orthogonal spatial matrix (V) and the orthogonal temporal matrix (T).

$$x_{ij} = \sum\nolimits_{k=1}^{m} v_{ik}t_{kj} = v_{i1}t_{1j} + v_{i2}t_{2j} + \cdots + v_{im}t_{mj} \tag{9}$$

Its matrix form is:

$$X = VT \tag{10}$$

The space matrix can be derived from the eigenvectors of XX^T.

$$C = XX^T = VTT^TV^T \tag{11}$$

Since the matrix C is a symmetric matrix, there must be:

$$C = V\Lambda V^T \tag{12}$$

The columns of matrix V are the eigenvectors of matrix C, and Λ is the diagonal matrix composed of the eigenvalues of C. The temporal matrix can be obtained once V is determined.

$$T = V^TX \tag{13}$$

The EOF decomposition results for VPD, SM_{root}, and SM_{surf} were obtained by utilizing the EOF package in Python 3.8.

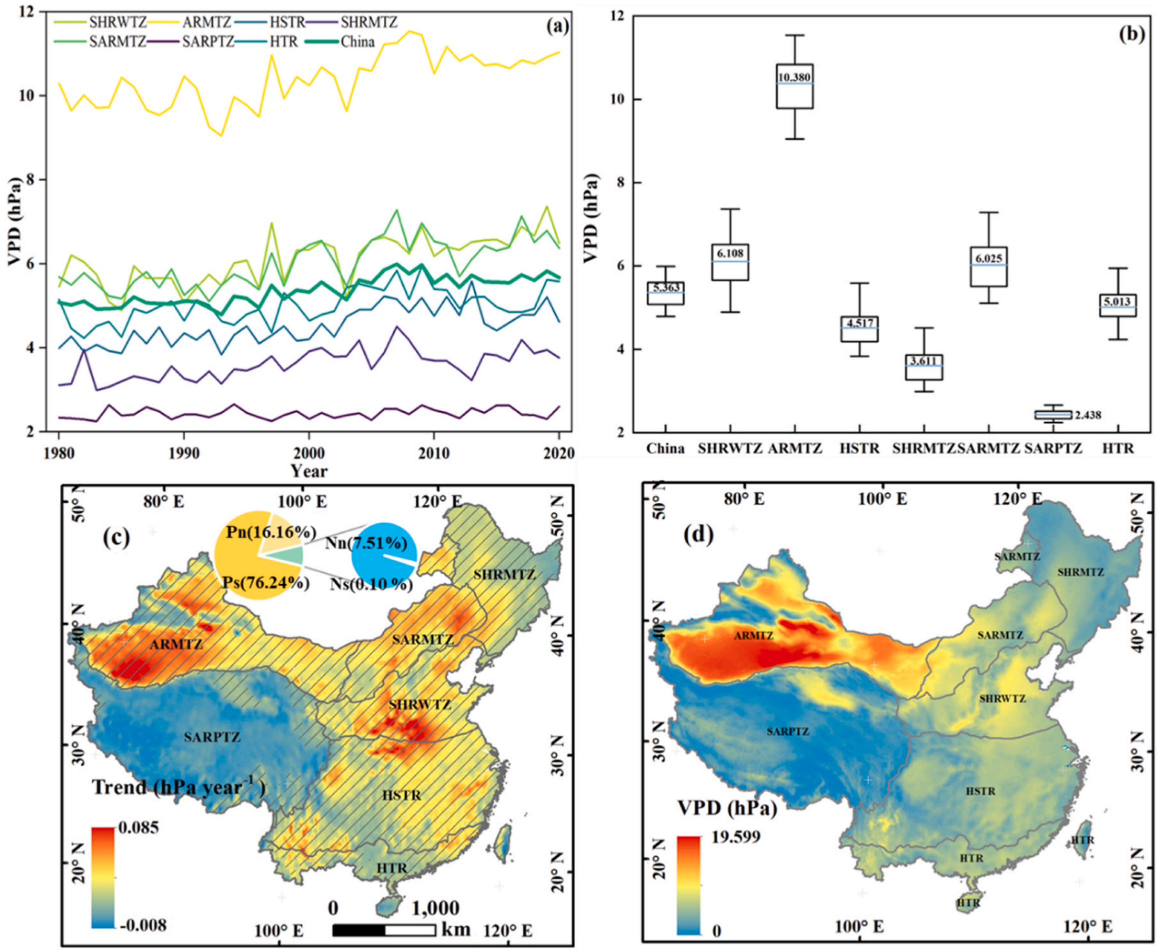

Fig. 3. Temporal change in mean VPD from 1980 to 2020. (a) Temporal change in VPD for China as well as individual climatic zones. (b) Average trends in VPD for China and different climatic zones. The blue solid lines in the boxes indicate the mean values. (c) Spatial distribution of VPD trends, with inserted pie charts indicating Ps (positive significant), Pn (positive non-significant), Ns (negative significant), and Nn (negative non-significant). (d) Spatial distribution of annual mean VPD. Slash indicates a positive trend for those passing the test, while a cross indicates a negative trend for those passing the test.

Table 2
Average trend values for different climate zones.

Climate zones	VPD		SM_{surf}		SM_{root}	
	Trend	P value	Trend	P value	Trend	P value
SHRWTZ	0.033	**	0.00045	**	0.00036	-
ARMTZ	0.034	**	0.00058	**	0.00047	**
HSTR	0.026	**	-0.00037	**	-0.00037	**
SHRMTZ	0.021	**	-0.00032	-	-0.00040	-
SARMTZ	0.034	**	0.00023	-	0.00023	-
SARPTZ	0.004	*	0.00026	**	0.00037	**
HTR	0.019	**	-0.00026	-	-0.00025	-
China	0.022	**	0.00012	-	0.00008	-

3. Results

3.1. Evaluation of VPD

The ERA5-land derived VPD was assessed against in situ observations and found to perform well, with an R^2 of 0.81 (Fig. 2a). Furthermore, at the monthly scale, the correlation coefficients between ERA5-land calculated VPD and in-situ derived VPD were

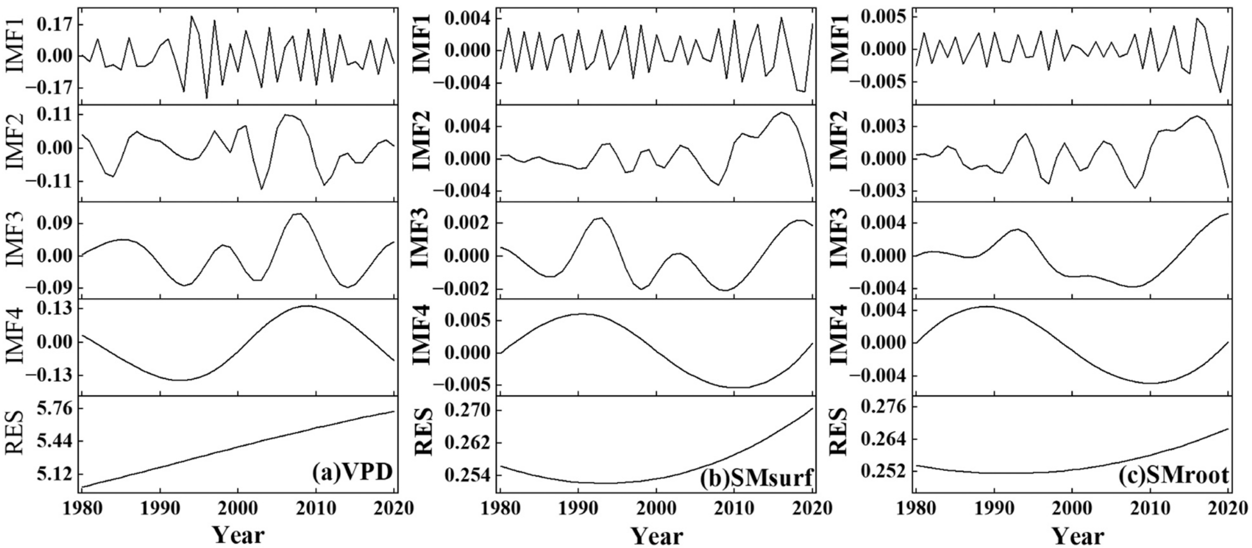

Fig. 4. Non-linear variation in interannual trends of VPD (a), SM_{surf} (b), SM_{root} (c) during 1980–2020.

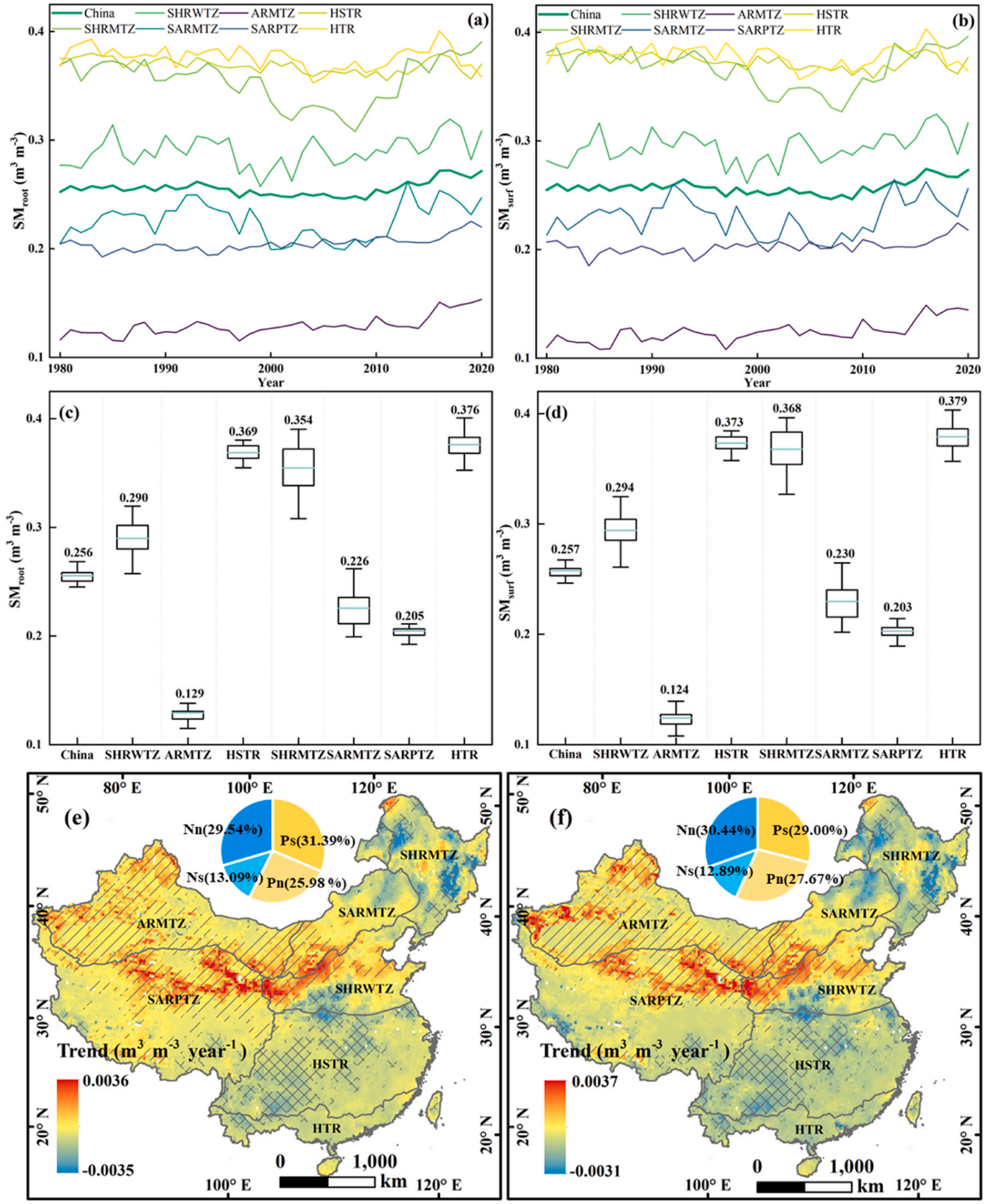

Fig. 5. Temporal changes in mean SM_{root} and SM_{surf} from 1980 to 2020. (a) and (b) temporal change in SM_{root} and SM_{surf} for China and individual climatic zones. (c) and (d) average trends in SM_{root} and SM_{surf} for China and different climatic zones. The blue solid lines in the boxes indicate the mean values. (e) and (f) spatial distribution of trends in SM_{root} and $SM_{surf,}$ with inserted pie charts indicating Ps (positive significant), Pn (positive non-significant), Ns (negative significant), Nn (negative non-significant). A slash indicates a positive trend for those passing the test, while a cross indicates a negative trend for those passing the test in the grid map.

consistently above 0.7 (Fig. 2c). Although there was a slight underestimation VPD (slope $<$ 1.0 and 5.03 vs. 4.55) compared to the in-situ measurements (Fig. 2a and b), the spatial assessment of VPD derived from ERA5-land exhibited a high level of consistency (Fig. 2d).

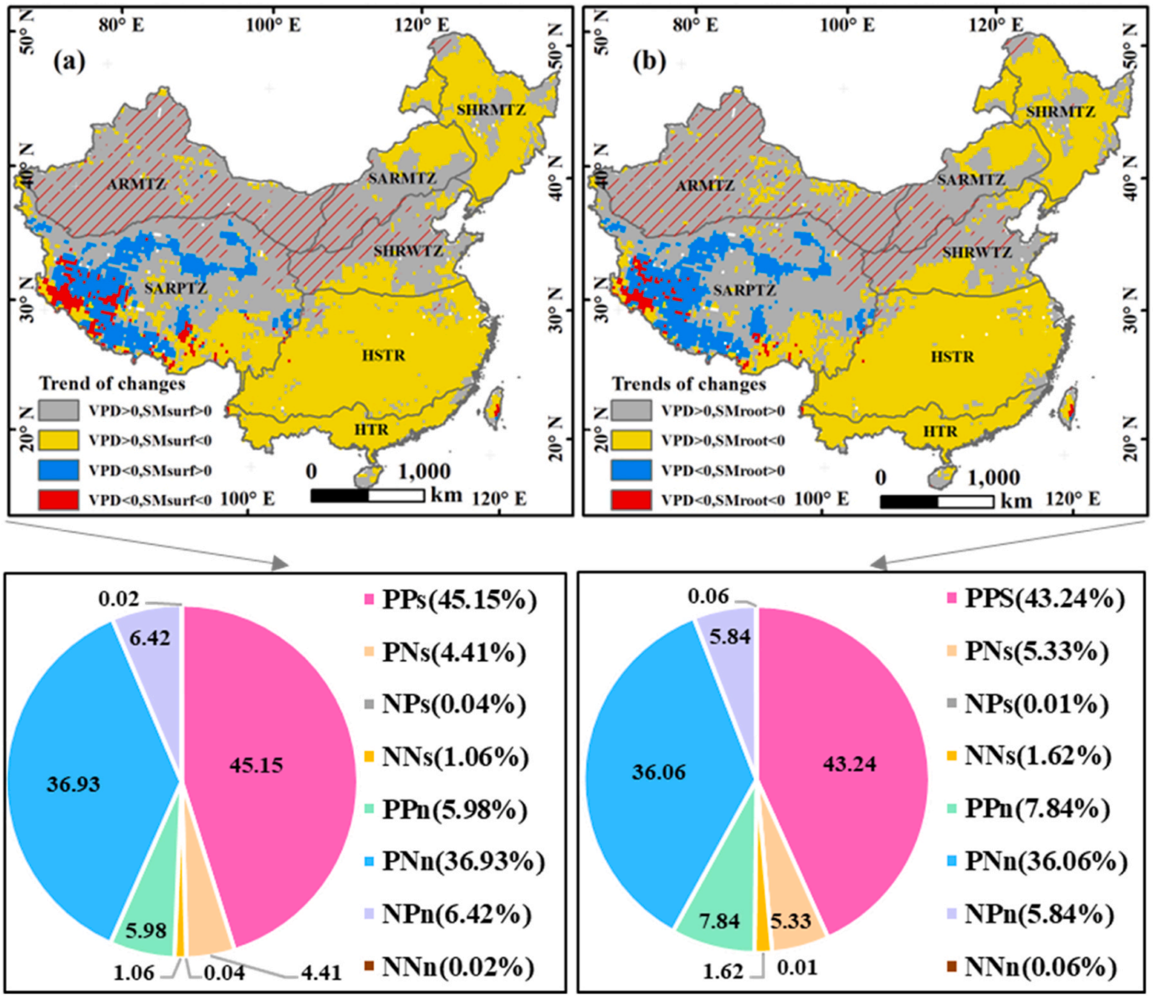

Fig. 6. VPD and SM trends combined. (a) VPD and SM_{surf} trends; (b) VPD and SM_{root} trends. A slash in red (/) indicates that VPD and SM_{surf}/ SM_{root} have passed the test. PPs, positive-positive significant; PPn, positive-positive non-significant; PNs, positive-negative significant; PNs, positive-negative non-significant; NPs, negative-positive significant; NPn, negative-positive non-significant; NNs, negative-negative significant; NNn, negative-negative non-significant. The percentages inside the parentheses represent the proportion of each type relative to the total.

3.2. VPD and SM of temporal variation

3.2.1. VPD of temporal variation

VPD showed a rising trend in China, with varying rates of increase observed across different climatic zones (Fig. 3c). Specifically, the arid zone (ARMTZ) experienced the highest rate of increase (0.034), while the semi-arid zone (SARPTZ) exhibited a comparatively slower rising trend (0.004) (Table 2). The mean VPD value in China was 5.363 hPa, with the highest values observed in ARMTZ (10.380 hPa) and the lowest in SARPTZ (2.438 hPa) (Fig. 3b). To investigate the non-linear variation of VPD, this study employed EEMD to decompose the VPD time series into four eigenmode components (IMF) and a trend term (RES), effectively filtering out noise and short-term seasonal trends (Fig. 4). The IMF1-IMF4 components represent distinct quasi-periods ranging from high-frequency to low-frequency in the original time series, capturing the corresponding nonuniform oscillations. The RES indicates the overall trend of the VPD time series during the study period. Our findings revealed a non-linear increasing trend in VPD over the past 41 years (Fig. 4a). Furthermore, the EEMD analysis revealed that VPD exhibited average periods of 2.6a (IMF1), 6.8a (IMF2), and 13.7a (IMF3) on the interannual scale.

3.2.2. SM of temporal variation

Both SM_{root} and SM_{surf} showed an increasing trend across China, although the trends varied across different climatic zones (Fig. 5e and f, Table 2). Notably, SM_{surf} exhibited declining trends in SHRWTZ, HSTR, and HTR, while demonstrating increasing trends in the other climate zones. ARMTZ had the lowest values for both SM_{root} and SM_{surf}, while HTR had the highest (Fig. 5c and d). The EEMD analysis revealed a non-linear increasing trend in both SM_{surf} and SM_{root} over the past 41 years (Fig. 4b and c). Furthermore, the results

Table 3
The variance contribution rate, cumulative variance contribution rate, eigenvalue, and errors for the first three modes of VPD, SM_{surf}, and SM_{root}.

Variables	Modes	Variance contribution rate (%)	Cumulative variance contribution rate (%)	Eigenvalue	Typical errors
VPD	1	48.52	48.52	12,943.32	2858.70
	2	8.69	57.21	2318.76	512.13
	3	7.47	64.67	1992.42	440.05
SM_{surf}	1	23.00	23.00	1.08	0.24
	2	17.61	40.61	0.83	0.18
	3	8.76	49.37	0.41	0.09
SM_{root}	1	25.92	25.92	1.24	0.27
	2	17.62	43.53	0.84	0.19
	3	8.71	52.25	0.42	0.09

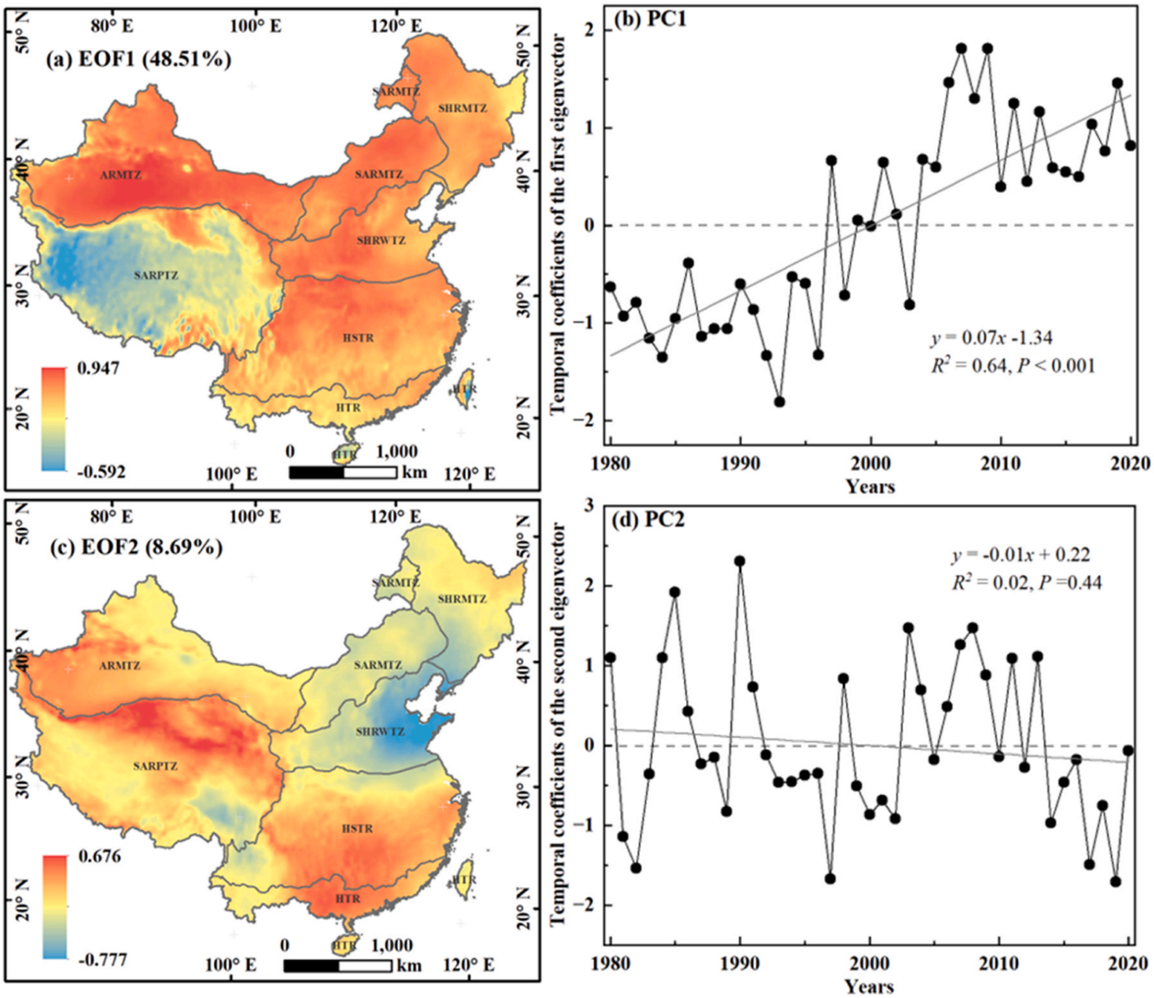

Fig. 7. Eigenvectors and their corresponding time coefficients of VPD by EOF. (a) first eigenvector; (b) time coefficients corresponding to the first eigenvector; (c) second eigenvector; (d) time coefficients corresponding to the second eigenvector.

indicated periodic variations in both SM_{surf} and SM_{root} on an interannual scale. SM_{surf} showed average periods of 2.7a (IMF1), 5.8a (IMF2), and 13.7a (IMF3), while SM_{root} exhibited similar periodic variations, except for IMF2, which had an average period of 5.1a.

The areas showing increasing trends in VPD and SM_{root}, as well as VPD and SM_{surf}, were predominantly distributed in ARMTZ, SARMTZ, and SHRWTZ, constituting 51.08% and 51.12% of the total area, respectively. Of these, 45.14% exhibit significant changes in either VPD or SM_{surf}, and 43.24% in either VPD or SM_{root} (Fig. 6). Furthermore, 23.08% had significance in both VPD and SM_{surf}, and 21.72% had significance in both VPD and SM_{root}. In contrast, we identified areas in HTR, HSTR, and SHRMTZ where VPD increased while SM_{root} (or SM_{surf}) decreased, constituting 41.39% and 41.34% of the total area, respectively (Fig. 6). However, only 5.33% and 4.41% of these areas exhibited significant changes. Additionally, the trend of VPD was negative, while the trend of SM_{root} or SM_{surf} was

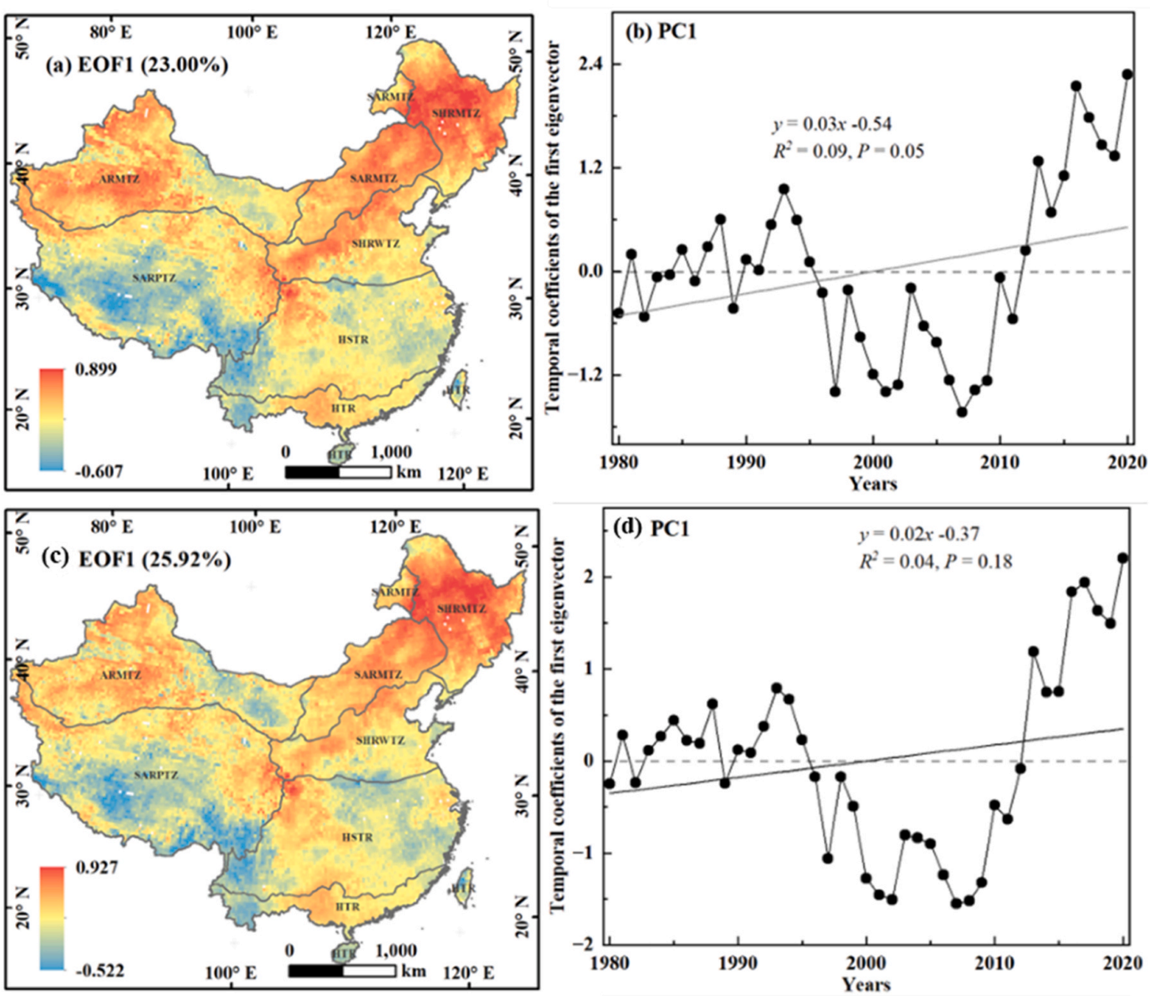

Fig. 8. Eigenvectors and their time coefficients of the SM_{surf} and SM_{root} by EOF during 1980–2020. (a) and (c) first eigenvector of SM_{surf} and SM_{root}, respectively; (b) and (d) time coefficients of SM_{surf} and SM_{root}.

positive, accounting for 5.86% and 6.46%, respectively. Of these, 0.01% exhibit significant changes in either VPD or SM_{surf} and 0.04% in either VPD or SM_{root}. The proportions of negative trends in VPD and SM_{root}, as well as VPD and SM_{surf}, are 1.68% and 1.08%, respectively. Of these, 1.62% exhibit significant changes in either VPD or SM_{surf} and 1.06% in either VPD or SM_{root}. However, in these significant regions, only 0.013% exhibit significant trends in both VPD and SM_{surf}, with 0.006% showing significant changes in both VPD and SM_{root}.

3.3. VPD and SM of spatial variation

EOF analysis was performed on the annual mean VPD, SM_{surf}, and SM_{root} in China over 41 years (1980–2020). Table 3 shows the top three eigenvalues for VPD, SM_{surf}, and SM_{root}. Among these values, only the first two eigenvalues passed the North significance test. The cumulative variance contribution rate of the first two modes for VPD was 57.21%, with variance contribution rates of 48.52% and 8.69% for the first two modes, respectively. Regarding SM_{surf} and SM_{root}, only EOF1 showed statistical significance in Chia, and therefore only the EOF1 was presented here.

3.3.1. VPD of spatial variation

Fig. 7 exhibited the spatial distribution (EOF) and the time coefficients (PC) of the first two modes. In EOF 1 (Fig. 7a), significantly large negative values appeared in the Qinghai-Tibet Plateau (SARPTZ). On the other hand, significantly large positive values appeared in the ARMTZ, which served as the center of positive values, implying the most sensitive areas to VPD variations. Fig. 7b illustrates the steady rise of time coefficients (from negative to positive) from 1980 to 2020. This trend indicated a decline in VPD in areas with significantly large negative values (e.g., SARPTZ) and an increase in VPD in areas with significantly large positive values (e.g., ARMTZ) over the past 41 years. The results were consistent with the annual trend of VPD variations (Fig. 3c).

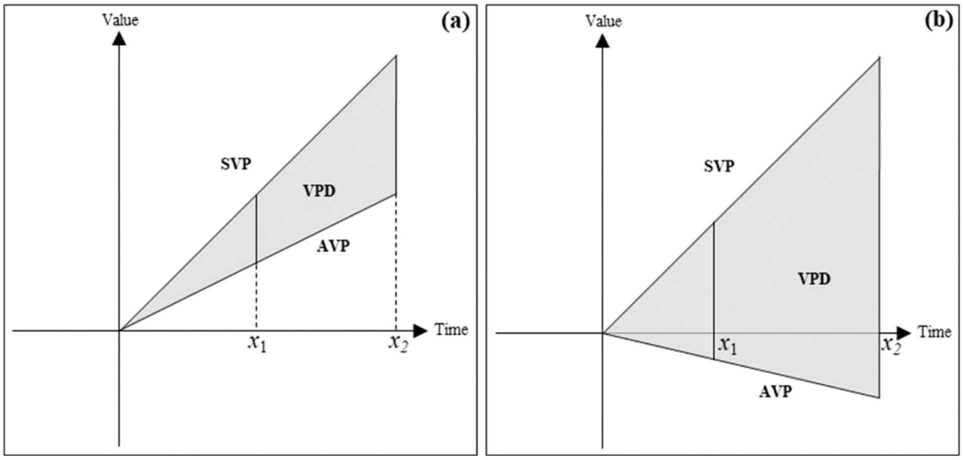

Fig. 9. The form of VPD change in case of temperature rise.

EOF2 reflected the local characteristics of VPD (Fig. 7c), displaying two distinct spatial patterns: positive and negative variations. The positive high-value zones were found in the SARPTZ, HSTR, and HTR, while the negative high-value regions appeared in the SHRWTZ. This inverse variation characteristic accounted for 8.69% of the overall variance. The temporal changes of the EOF2 time coefficients were depicted in Fig. 7d. In the years with positive time coefficients, the atmosphere in the SHRWTZ was increasingly humid, and the atmosphere in the SARPTZ, HSTR, and HTR was drier.

3.3.2. SM of spatial variation

The EOF decomposition results for SM_{root} and SM_{surf} in the study area were similar, indicating consistent spatial variation characteristics of SM_{root} and SM_{surf} over the past 41 years. Fig. 8a (Fig. 8c) illustrates the spatial distribution of EOF1 for SM_{surf} (SM_{root}) in China. The positive values of EOF1 were observed in all regions except SARPTZ, indicating a consistent annual variation pattern of SM_{surf} (SM_{root}). This characteristic accounted for 23% (25.92%) of the overall variance. Notably, the high values of SM_{surf} variation were in the SHRMTZ, indicating that the area was the most sensitive to soil moisture variation.

In Fig. 8b and d, the time coefficients associated with EOF1 depict the interannual trend variation of SM_{surf} and SM_{root}, respectively. While the time coefficients showed an overall increasing trend, the interannual fluctuations were obvious. Before 1995, the time coefficients alternated between positive and negative values, followed by a negative trend from 1995 to 2010. However, the coefficients turned positive again after 2010. These patterns suggest that the overall soil moisture in the study area has been progressing toward increased humidity over the past 40 years.

4. Discussion

4.1. Increasing atmospheric moisture scarcity

Significant increases in VPD were observed across various regions in China over the past 40 years (Figs. 3c and 7). These findings indicate a persistent and escalating trend of atmospheric drought. The rise in VPD can be primarily attributed to the increase in air temperature. Higher temperatures cause an elevation in saturated vapor pressure, as per the Clausius-Clapeyron relation (Chen et al., 2011). In the context of rising temperatures, the increase in VPD can occur in two scenarios based on the VPD formula: 1) the rate of increase in SVP exceeds the rate of increase in AVP (Fig. 9a); 2) SVP is increasing while AVP is decreasing (Fig. 9b). The increase in SVP was mainly attributed to air temperature (De Boeck et al., 2010). On the other hand, the variation in AVP was influenced by multiple factors, including air temperature, evaporation, RH, and SM (Fang et al., 2022; Ficklin and Novick, 2017), as we found that VPD was correlated with multiple factors. Specifically, air temperature exhibited a strong positive correlation with VPD. Conversely, RH displayed a strong negative correlation with VPD. And SM_{surf} showed a slight negative correlation with VPD. The rise in temperature led to an increase in SVP. Across China, 99.94% of regions exhibited a rising temperature trend (Fig. 11a), and 99.91% of regions showed an increase in SVP. However, 79.56% of the regions experienced a decline in RH, and total evaporation showed a decreasing trend, implying a reduction in atmospheric moisture. The change in RH influences the rate of AVP shifts. AVP was increasing in 76.53% of China's areas while decreasing in the remaining regions. This indicates that two scenarios are contributing to the increase in VPD in China, with the first scenario being more prevalent. In this study, we found that 76.53% of the regions experienced an increase in AVP, while 23.47% witnessed a decrease across China. For SVP, 99.91% of the regions showed an increase, with only 0.09% experiencing a decrease. Building upon this, we conducted a further analysis on the proportions of concurrent increases in SVP and AVP, as well as increases in SVP with decreases in AVP (76.45% and 23.46%, respectively, Fig. 11l). This suggests that the primary trend in the variation of the VPD in China aligns with the first scenario. Additionally, we observed that the average growth rate of SVP was nearly six times that of AVP. This phenomenon is also evident on a global scale, where the increase in VPD is largely attributed to the

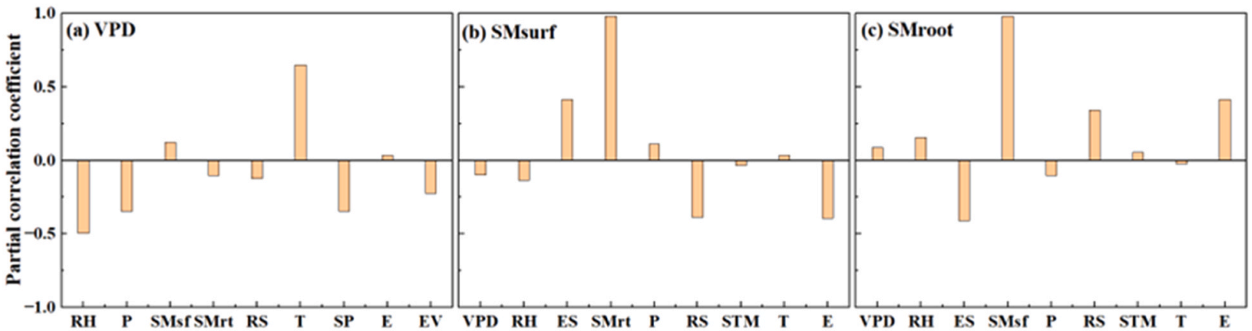

Fig. 10. Partial correlation analysis of environmental variables with (a) VPD, (b) SM_{surf}, and (c) SM_{root}. E, evaporation; P, precipitation; TM, temperature; SP, surface pressure; SR, downwelling shortwave radiation; EV, vegetation evaporation; ES, soil evaporation; STM, soil temperature 0–7 cm; RH, relative moisture.

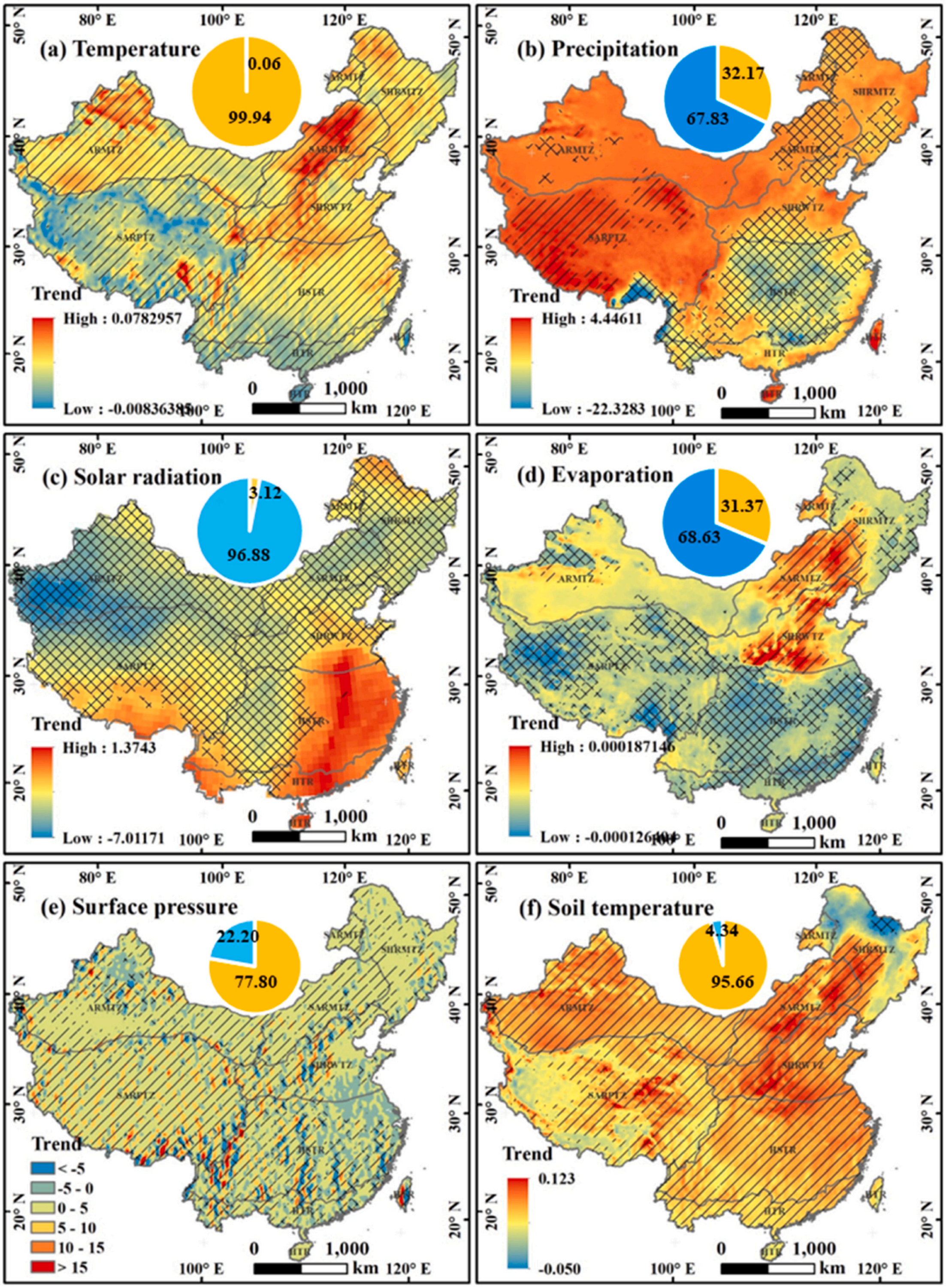

Fig. 11. Trends in climate factors during 1980–2020.

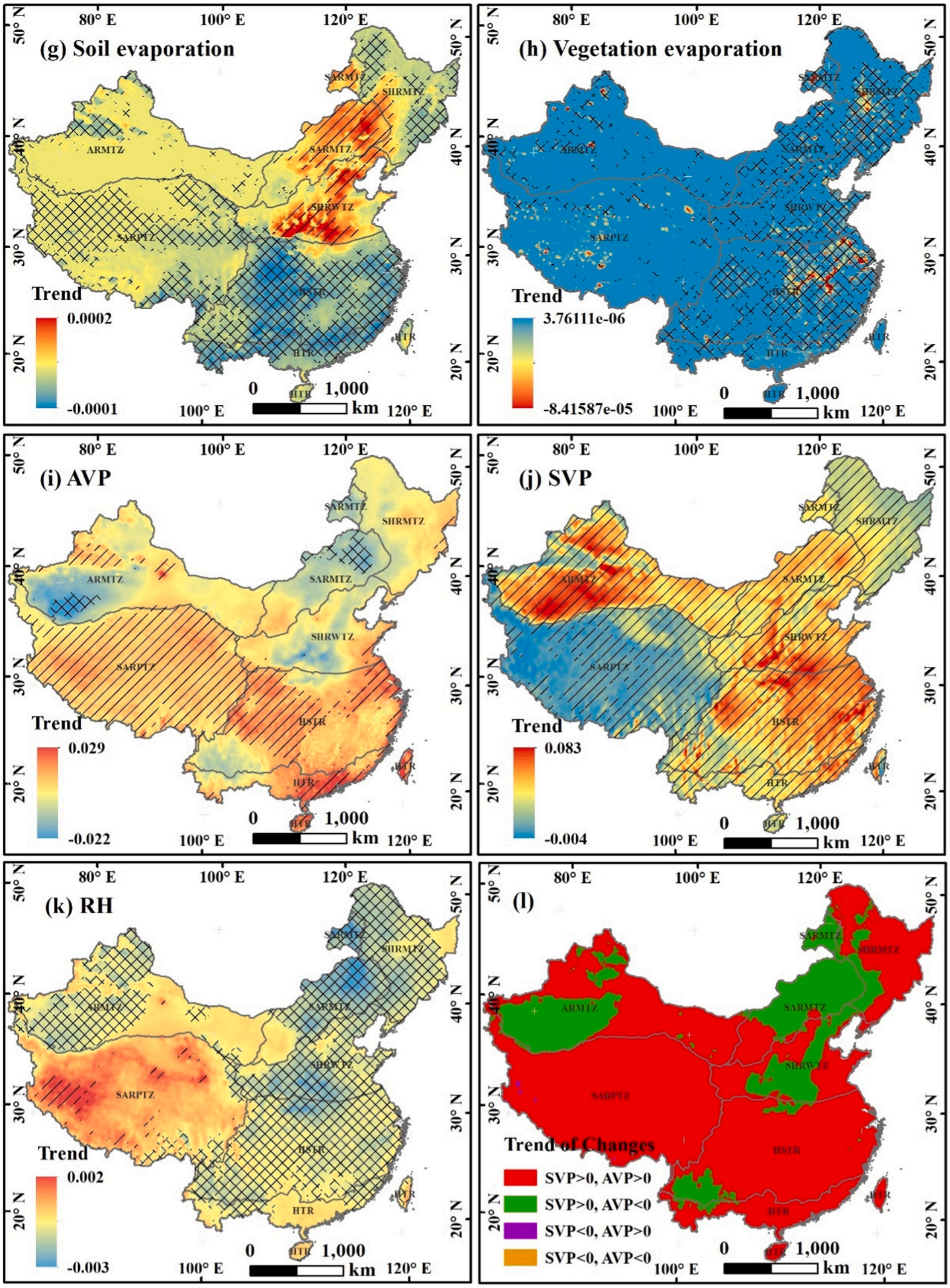

Fig. 11. (*continued*).

Table 4
Proportion of positive and negative trend values in different climatic zones.

Climate zones	Trend	E	ES	EV	P	SP	STM	SR	T	AVP	RH	SVP
HTR	>0	5.01	3.15	6.64	10.35	64.43	100.00	14.75	100.00	93.91	3.96	99.96
	<0	94.99	96.85	93.36	89.65	35.57	0.00	85.25	0.00	6.09	96.04	0.04
HSTR	>0	5.06	3.21	0.00	1.59	60.26	100.00	11.66	99.99	90.61	0.41	99.99
	<0	94.94	96.79	100.00	98.41	39.74	0.00	88.34	0.01	9.39	99.59	0.01
SHRMTZ	>0	23.55	21.60	0.00	2.02	86.19	68.13	0.00	100.00	79.66	0.00	100.00
	<0	76.45	78.40	100.00	97.98	13.81	31.87	100.00	0.00	20.34	100.00	0.00
SHRWTZ	>0	82.00	79.83	0.04	7.42	69.74	100.00	2.08	100.00	58.45	0.00	100.00
	<0	18.00	20.17	99.96	92.58	30.26	0.00	97.92	0.00	41.55	100.00	0.00
SARMTZ	>0	86.16	84.98	0.00	13.08	90.36	96.41	0.00	100.00	21.81	0.03	100.00
	<0	13.84	15.02	100.00	86.92	9.64	3.59	100.00	0.00	78.19	99.97	0.00
SARPTZ	>0	3.60	9.01	3.25	83.13	85.39	98.37	0.00	99.77	99.05	75.39	99.68
	<0	96.40	90.99	96.75	16.87	14.61	1.63	100.00	0.23	0.95	24.61	0.32
ARMTZ	>0	52.70	29.71	0.17	37.54	80.88	100.00	0.00	100.00	62.46	2.32	100.00
	<0	47.30	70.29	99.83	62.46	19.12	0.00	100.00	0.00	37.54	97.68	0.00

deceleration in the growth rate of AVP (Xu et al., 2024).

4.2. SM showed divergent trends

Fig. 10 SM serves as a reliable indicator of soil drought conditions. Given the growing prominence of atmospheric drought, it becomes crucial to assess the soil drought condition. This is essential because SM plays a significant role in supporting vegetation growth, as highlighted in previous studies (Collins et al., 2018; Yu et al., 2022). We found a slight overall increase across China. Specifically, SM exhibited an increase in regions such as ARMTZ, SARMTZ, SHRWTZ, and SARPTZ. However, we observed a decrease in SM in the HSTR, HTR, and SHRMTZ regions. These divergent changes reflected a polarization phenomenon in soil moisture dynamics. The slight increase in SM in China, occurring alongside rising temperatures, can be attributed to various factors, including evaporation, precipitation, and solar radiation (Fig. 11). Previous studies have highlighted the significance of evaporation and precipitation in influencing SM dynamics (Cheng et al., 2015; Cheng and Huang, 2016; Liu and Yang, 2023). Based on the results of partial correlation analysis (Fig. 10), evaporation showed a negative correlation with soil moisture (SM), while precipitation exhibited a positive correlation. This implies that a decrease in evaporation and an increase in precipitation both contribute to the increase in SM. We found that the rise in soil moisture (SM) in SARPTZ can be attributed to increased precipitation and decreased evaporation, as shown in Table 4. Additionally, another factor could contribute to an increase in soil and air temperature. This leads to permafrost melting and increases soil water content, which raises SM levels (Chen et al., 2022; Li et al., 2020). The increase in SM in ARMTZ cannot be solely attributed to precipitation, as indicated by the decreasing trend in 62.46% of ARMTZ precipitation values (Table 4). Instead, it is likely due to a combination of factors. Firstly, the decrease in solar radiation leads to a reduction in evaporation, resulting in less soil moisture loss. Additionally, the recovery of vegetation in arid regions and the increase in water content may also contribute to the preservation of SM (Liu and Yang, 2023; Zhang et al., 2022a). In SHRMTZ, the decrease in SM can be attributed to the declining precipitation. Moreover, the HTR and HSTR regions experience a more pronounced decrease in precipitation. Despite the decrease in evaporation, which would lead to a decrease in SM, the significant role of precipitation as a driver of SM change is evident. Conversely, in SHRWTZ, the increase in SM is likely a result of reduced evaporation. The observed increase in soil moisture (SM) in SARMTZ is not adequately explained by the concurrent decrease in precipitation and increase in evaporation. The current changes in these climate factors do not provide a clear explanation for the observed phenomenon. Further investigation is needed to understand the underlying mechanisms driving the SM increase in SARMTZ.

5. Conclusion

Main findings of the paper: In this study, we conducted a comprehensive investigation into the spatial-temporal variations of VPD and SM in China. We found a significant increase in VPD across China, with particularly pronounced trends observed in the ARMTZ, SARMTZ, and SHRWTZ regions. As for SM, we found an overall increase in both SM_{surf} and SM_{root} in China. However, there was variability in different climate zones. Notably, the HTR, HSTR, and SHRMTZ regions exhibited a decreasing trend in SM_{surf} and SM_{root}, whereas the other climate zones exhibited an upward trend. In the ARMTZ and SRAMTZ, both VPD and SM showed an increasing trend. These results indicate a general trend of increasing aridity in the atmosphere and a gradual moistening of the soil in response to rising temperature.

Limitations of this work: We employed the EEMD and EOF methods to analyze the spatiotemporal dynamics of VPD and SM and explored the underlying reasons. Our analysis mainly focused on climatic factors to understand the causes of VPD and SM changes, without considering atmospheric circulation factors and ocean temperatures. Nonetheless, some studies suggest that changes in ocean temperatures may also contribute to VPD variations (Yuan et al., 2019).

Broader impacts: As the climate warms, droughts are becoming more frequent and severe, making the arid and semi-arid regions a research hotspot. Our study reveals decreasing soil moisture and increasing VPD in humid and semi-humid areas, indicating shifts in the atmospheric-soil moisture dynamics of these regions. This shift requires attention for its potential impacts on the ecosystems of these areas in the future.

CRediT authorship contribution statement

Shanshan Chen: Writing – review & editing, Writing – original draft, Validation, Methodology, Formal analysis, Data curation, Conceptualization. **Songlin Zhang:** Writing – review & editing, Data curation. **Shengjun Wu:** Writing – review & editing, Supervision, Resources, Conceptualization.

Declaration of Competing Interest

The authors declare that they have no financial conflict of interest.

Data availability

Data will be made available on request.

Acknowledgments

This research was financially supported by the National Natural Science Foundation of China (Grant No. 42371071), China Postdoctoral Science Foundation (2021M703137), Chongqing Postdoctoral Science Foundation (cstc2021jcyj-bshX0195), and the Three Gorges' follow-up scientific research project from Chongqing Municipal Bureau of Water Resources (No. 5000002021BF40001).

Appendix A. Supporting information

Supplementary data associated with this article can be found in the online version at doi:10.1016/j.ejrh.2024.101712.

References

Ameztegui, A., Morán-Ordóñez, A., Márquez, A., Blázquez-Casado, Á., Pla, M., Villero, D., García, M.B., Errea, M.P., Coll, L., 2021. Forest expansion in mountain protected areas: trends and consequences for the landscape. Land. Urban Plan. 216, 104240 https://doi.org/10.1016/j.landurbplan.2021.104240.

Beck, H.E., Pan, M., Miralles, D.G., Reichle, R.H., Dorigo, W.A., Hahn, S., Sheffield, J., Karthikeyan, L., Balsamo, G., Parinussa, R.M., van Dijk, A.I.J.M., Du, J., Kimball, J.S., Vergopolan, N., Wood, E.F., 2021. Evaluation of 18 satellite- and model-based soil moisture products using in situ measurements from 826 sensors. Hydrol. Earth Syst. Sci. 25 (1), 17–40. https://doi.org/10.5194/hess-25-17-2021.

Berg, A., Sheffield, J., Milly, P.C.D., 2017. Divergent surface and total soil moisture projections under global warming. Geophys. Res. Lett. 44 (1), 236–244. https://doi.org/10.1002/2016GL071921.

Chen, G., Ming, Y., Singer, N.D., Lu, J., 2011. Testing the Clausius-Clapeyron constraint on the aerosol-induced changes in mean and extreme precipitation. Geophys. Res. Lett. 38 (4), L04807. https://doi.org/10.1029/2010GL046435.

Chen, J., Wu, T.H., Liu, L., Gong, W.Y., Zwieback, S., Zou, D., Zhu, X.F., Hu, G.J., Du, E.J., Wu, X.D., Li, R., Yang, S.Z., 2022. Increased water content in the active layer revealed by regional-scale inSAR and independent component analysis on the central Qinghai-Tibet Plateau. e2021GL097586 Geophys. Res. Lett. 49 (15). https://doi.org/10.1029/2021GL097586.

Chen, X.Z., Ciais, P., Maignan, F., Zhang, Y., Bastos, A., Liu, L.Y., Bacour, C., Fan, L., Gentine, P., Goll, D., Green, J., Kim, H., Li, L., Liu, Y., Peng, S., Tang, H., Viovy, N., Wigneron, J.P., Wu, J., Yuan, W.P., Zhang, H.C., 2021. Vapor pressure deficit and sunlight explain seasonality of leaf phenology and photosynthesis across amazonian evergreen broadleaved forest. e2020GB006893 Glob. Biogeochem. Cycles 35 (6). https://doi.org/10.1029/2020GB006893.

Cheng, S.J., Huang, J.P., 2016. Enhanced soil moisture drying in transitional regions under a warming climate. J. Geophys. Res. Atmos. 121 (6), 2542–2555. https://doi.org/10.1002/2015JD024559.

Cheng, S.J., Guan, X.D., Huang, J.P., Ji, F., Guo, R.X., 2015. Long-term trend and variability of soil moisture over East Asia. J. Geophys. Res. Atmos. 120 (17), 8658–8670. https://doi.org/10.1002/2015JD023206.

Collins, L., Bradstock, R.A., Resco de Dios, V., Duursma, R.A., Velasco, S., Boer, M.M., 2018. Understorey productivity in temperate grassy woodland responds to soil water availability but not to elevated CO_2. Glob. Chang. Biol. 24 (6), 2366–2376. https://doi.org/10.1111/gcb.14038.

De Boeck, H.J., Dreesen, F.E., Janssens, I.A., Nijs, I., 2010. Climatic characteristics of heat waves and their simulation in plant experiments. Glob. Chang. Biol. 16 (7), 1992–2000. https://doi.org/10.1111/j.1365-2486.2009.02049.x.

Deng, L., Wang, K.B., Li, J.P., Zhao, G.W., Shangguan, Z.P., 2016. Effect of soil moisture and atmospheric humidity on both plant productivity and diversity of native grasslands across the Loess Plateau, China. Ecol. Eng. 94, 525–531. https://doi.org/10.1016/j.ecoleng.2016.06.048.

Fang, Z.X., Zhang, W.M., Brandt, M., Abdi, A.M., Fensholt, R., 2022. Globally increasing atmospheric aridity over the 21st century. e2022EF003019 Earths Future 10 (10). https://doi.org/10.1029/2022EF003019.

Ficklin, D.L., Novick, K.A., 2017. Historic and projected changes in vapor pressure deficit suggest a continental-scale drying of the United States atmosphere. J. Geophys. Res. Atmos. 122 (4), 2061–2079. https://doi.org/10.1002/2016JD025855.

Gatti, L.V., Gloor, M., Miller, J.B., Doughty, C.E., Malhi, Y., Domingues, L.G., Basso, L.S., Martinewski, A., Correia, C.S.C., Borges, V.F., Freitas, S., Braz, R., Anderson, L.O., Rocha, H., Grace, J., Phillips, O.L., Lloyd, J., 2014. Drought sensitivity of Amazonian carbon balance revealed by atmospheric measurements. Nature 506 (7486), 76–80. https://doi.org/10.1038/nature12957.

Green, J.K., Seneviratne, S.I., Berg, A.M., Findell, K.L., Hagemann, S., Lawrence, D.M., Gentine, P., 2019. Large influence of soil moisture on long-term terrestrial carbon uptake. Nature 565, 476–479. https://doi.org/10.1038/s41586-018-0848-x.

Huang, N.E., Shen, Z., Long, S.R., Wu, M.C., Shih, H.H., Zheng, Q., Yen, N.-C., Tung, C.C., Liu, H.H., 1998. The empirical mode decomposition and the Hilbert spectrum for nonlinear and non-stationary time series analysis. Proc. R. Soc. Lond. A 454 (1971), 903–995.

Kong, X., Guan, X., Cao, C., Zhang, T., Shen, L., Gan, Z., Ma, J., Huang, H., 2019. Decadal change in soil moisture over East Asia in response to a decade-long warming hiatus. J. Geophys. Res. Atmos. 124 (15), 8619–8630. https://doi.org/10.1029/2019JD030294.

Levitus, S., Antonov, J.I., Boyer, T.P., Garcia, H.E., Locarnini, R.A., 2005. EOF analysis of upper ocean heat content, 1956-2003. Geophys. Res. Lett. 32 (18), L18607. https://doi.org/10.1029/2005GL023606.

Li, D.F., Li, Z.W., Zhou, Y.J., Lu, X.X., 2020. Substantial increases in the water and sediment fluxes in the headwater region of the Tibetan Plateau in response to global warming. e2020GL087745 Geophys. Res. Lett. 47 (11). https://doi.org/10.1029/2020GL087745.

Liu, H.Y., Zhang, M.Y., Lin, Z.S., Xu, X.J., 2018. Spatial heterogeneity of the relationship between vegetation dynamics and climate change and their driving forces at multiple time scales in Southwest China. Agric. For. Meteorol. 256-257, 10–21.

Liu, Y.X.Y., Yang, Y.P., 2023. Spatial-temporal variability pattern of multi-depth soil moisture jointly driven by climatic and human factors in China. J. Hydrol. 619, 129313 https://doi.org/10.1016/j.jhydrol.2023.129313.

Lu, H., Qin, Z., Lin, S., Chen, X., Chen, B., He, B., Wei, J., Yuan, W., 2022. Large influence of atmospheric vapor pressure deficit on ecosystem production efficiency. Nat. Commun. 13 (1), 1653. https://doi.org/10.1038/s41467-022-29009-w.

Mao, R., Kim, S.J., Gong, D.Y., Liu, X.H., Wen, X.Y., Zhang, L.P., Tang, F., Zong, Q., Xiao, C.D., Ding, M.H., Park, S.J., 2021. Increasing difference in interannual summertime surface air temperature between interior east Antarctica and the Antarctic Peninsula under future climate scenarios. e2020GL092031 Geophys. Res. Lett. 48 (16). https://doi.org/10.1029/2020GL092031.

Martens, B., Miralles, D.G., Lievens, H., van der Schalie, R., de Jeu, Fernández-Prieto, D., Beck, H.E., Dorigo, W.A., Verhoest, N.E.C., 2017. GLEAM v3: Satellite-based land evaporation and root-zone soil moisture. Geosci. Model Dev. 10 (5), 1903–1925.

Miralles, D.G., Holmes, T.R.H., De Jeu, Gash, J.H., Meesters, A.G.C.A., Dolman, A.J., 2011. Global land-surface evaporation estimated from satellite-based observations. Hydrol. Earth Syst. Sci. 15 (2), 453–469.

Muñoz Sabater, J. (2019). ERA5-Land hourly data from 1981 to present. Copernicus Climate Change Service (C3S) Climate Data Store (CDS), 10.

Sangines de Carcer, P., Vitasse, Y., Penuelas, J., Jassey, V.E.J., Buttler, A., Signarbieux, C., 2018. Vapor-pressure deficit and extreme climatic variables limit tree growth. Glob. Chang. Biol. 24 (3), 1108–1122. https://doi.org/10.1111/gcb.13973.

Stocker, B.D., Zscheischler, J., Keenan, T.F., Prentice, I.C., Penuelas, J., Seneviratne, S.I., 2018. Quantifying soil moisture impacts on light use efficiency across biomes. New Phytol. 218 (4), 1430–1449. https://doi.org/10.1111/nph.15123.

Wang, T.J., Franz, T.E., Li, R.P., You, J.S., Shulski, M.D., Ray, C., 2017. Evaluating climate and soil effects on regional soil moisture spatial variability using EOFs. Water Resour. Res. 53 (5), 4022–4035. https://doi.org/10.1002/2017WR020642.

Wei, L., Zhou, H., Link, T.E., Kavanagh, K.L., Hubbart, J.A., Du, E., Hudak, A.T., Marshall, J.D., 2018. Forest productivity varies with soil moisture more than temperature in a small montane watershed. Agric. Meteor. 259, 211–221. https://doi.org/10.1016/j.agrformet.2018.05.012.

Winkler, D.E., Chapin, K.J., Kueppers, L.M., 2016. Soil moisture mediates alpine life form and community productivity responses to warming. Ecology 97 (6), 1553–1563. https://doi.org/10.1890/15-1197.1.

Xu, W.F., Xia, X.S., Piao, S.L., Wu, D.H., Li, W.B., Yang, S., Yuan, W.P., 2024. Weakened increase in global near-surface water vapor pressure during the last 20 years. e2023GL107909 Geophys. Res. Lett. 51. https://doi.org/10.1029/2023GL107909.

Yu, P.X., Zhou, T., Luo, H., Liu, X., Shi, P., Zhao, X., Xiao, Z.Q., Zhang, Y.J., Zhou, P.F., Disney, M., Zhang, J., 2022. Interannual variation of gross primary production detected from optimal convolutional neural network at multi-timescale water stress. Remote Sens. Ecol. Conserv. 8 (3), 409–425. https://doi.org/10.1002/rse2.252.

Yuan, W.P., Zheng, Y., Piao, S.L., Ciais, P., Lombardozzi, D., Wang, Y.P., Ryu, Y., Chen, G.X., Dong, W.J., Hu, Z.M., Jain, A.K., Jiang, C.Y., Kato, E., Li, S.H., Lienert, S., Liu, S.G., Nabel, J.E.M.S., Qin, Z.C., Quine, T., Sitch, S., Smith, W.K., Wang, F., Wu, C.Y., Xiao, Z.Q., Yang, S., 2019. Increased atmospheric vapor pressure deficit reduces global vegetation growth. Sci. Adv. 5 (8), eaax1396 https://doi.org/10.1126/sciadv.aax1396.

Zhang, B.Q., Tian, L., Yang, Y.T., He, X.G., 2022a. Revegetation does not decrease water yield in the Loess Plateau of China. e2022GL098025 Geophys. Res. Lett. 49 (9). https://doi.org/10.1029/2022GL098025.

Zhang, Y.H., Peng, X.X., Ning, F., Dong, Z.Y., Wang, R., Li, J., 2022b. Assessing the response of orchard productivity to soil water depletion using field sampling and modeling methods. Agric. Water Manag. 273, 107883 https://doi.org/10.1016/j.agwat.2022.107883.